Blood Flow in Abdominal Aortic Aneurysms: Pulsatile Flow Hemodynamics

Ender A. Finol
Mem. ASME

Cristina H. Amon
Raymond J. Lane Distinguished Professor.
Fellow ASME

Mechanical Engineering, Biomedical
and Health Engineering;
and Institute for Complex Engineered Systems,
Carnegie Mellon University,
Pittsburgh, PA 15213-3890

Numerical predictions of blood flow patterns and hemodynamic stresses in Abdominal Aortic Aneurysms (AAAs) are performed in a two-aneurysm, axisymmetric, rigid wall model using the spectral element method. Physiologically realistic aortic blood flow is simulated under pulsatile conditions for the range of time-averaged Reynolds numbers $50 \leqslant Re_m \leqslant 300$*, corresponding to a range of peak Reynolds numbers* $262.5 \leqslant Re_{peak} \leqslant 1575$*. The vortex dynamics induced by pulsatile flow in AAAs is characterized by a sequence of five different flow phases in one period of the flow cycle. Hemodynamic disturbance is evaluated for a modified set of indicator functions, which include wall pressure (*p_w*), wall shear stress (*τ_w*), and Wall Shear Stress Gradient (WSSG). At peak flow, the highest shear stress and WSSG levels are obtained downstream of both aneurysms, in a pattern similar to that of steady flow. Maximum values of wall shear stresses and wall shear stress gradients obtained at peak flow are evaluated as a function of the time-average Reynolds number resulting in a fourth order polynomial correlation. A comparison between predictions for steady and pulsatile flow is presented, illustrating the importance of considering time-dependent flow for the evaluation of hemodynamic indicators.* [DOI: 10.1115/1.1395573]

Introduction

Abdominal Aortic Aneurysms (AAAs) are localized balloon-shaped expansions commonly found in the infrarenal segment of the abdominal aorta, between the renal arteries and the iliac bifurcation. While the cause and nature of AAAs is still an important matter of debate, abdominal aortic aneurysm rupture is the 15th leading cause of death in the United States, affecting patients over 55 years of age, typically 2–4 percent of elderly males. As the overall mortality rate following aneurysm rupture may exceed 90 percent [1], determining the risk factors that may have an important role in aneurysm growth and rupture has become an integrated multidisciplinary task oriented toward obtaining a thorough understanding on the pathogenesis and evolution of AAAs. It is well known now that arterial diseases, present in local irregular geometries, are the result of a combination of complex biochemical processes that take place in the vascular wall at the cellular level as well as hemodynamic factors resulting from the interaction of blood flow and the inner wall. Recent investigations related to AAA phenomena are based on four major areas: (1) clinical studies focused on the etiology and screening of AAAs as well as the determination of possible risk factors related to chemical alterations occurring in the cellular matrix of the severely eroded tunica intima; (2) experimental and numerical studies focused on the simulation of physiological hemodynamics in aneurysm models; (3) experimental and numerical studies based on stress–strain analysis and wall mechanics of the aneurysm wall, and (4) in-vitro cell biology investigations and numerical simulations of cell models that attempt to correlate the hemodynamic patterns found in arterial models with the clinical evidence known for arterial diseases. It is the purpose of this work to provide new insights into hemodynamic indicators that may be of physiological importance when simulating blood flow, under pulsatile conditions, through abdominal aortic aneurysm models.

Experimental and numerical investigations of pulsatile flow in AAAs have been performed during the last and present decades. The first numerical study of pulsatile blood flow in aneurysms [2] demonstrated the presence of a vortex that varied in size and intensity during the cardiac cycle. Perktold et al. [3,4] represented pulsatile flow patterns with velocity vectors and particle paths through axisymmetric aneurysm models. The first combined experimental and numerical study of pulsatile flow in AAAs [5] showed the existence of primary and secondary vortices, and relatively high negative shear stresses and pressure fluctuations in the distal edge of the aneurysm. Three-dimensional unsteady flow simulations [6] resulted in predicting the appearance and disappearance of the primary vortex, and regions of high wall shear stresses both at the proximal and distal edge. Elger et al. [7] numerically simulated pulsatile flow, providing flow patterns and their effect on wall shear stresses and pressure distributions. Parametric studies demonstrated the little influence that the AAA bulge and the vortex structure have on pressure distributions. The flow frequency, however, has the most significant effect on the magnitudes of the wall pressure and shear stresses [8]. Correlation between steady blood flow dynamics and rates of platelet deposition proved the existence of a monotonic increase of platelet aggregation at the aneurysm wall, until reaching a maximum at the distal edge [9,10]. Guzmán and Amon [11] and Amon et al. [12] have studied the temporal flow evolution of laminar, transitional, and chaotic flow in converging–diverging channels using a geometry similar to that investigated in this work. Boundary layer separation during pulsatile flow has been seen ahead and behind the vortex regions within an aneurysm [13,14]. Direct numerical simulations of non-Newtonian flow through double-aneurysm models have been conducted under pulsatile conditions, resulting in flow patterns and wall shear stresses that were underestimated for otherwise Newtonian flow behavior [15,16]. Guzmán et al. [17] performed validation studies of pulsatile non-Newtonian flow simulations by means of three asymptotic cases that take into account geometric inhomogeneities in the model. Resting and exercise conditions were investigated both experimentally and numerically resulting in three distinct flow regimes of pulsatile blood flow in AAAs [18,19]. Peattie and Bluth [20] and Peattie et al. [21] suggest that aneurysm diameter has little effect on the wall pressure distribution and its magnitude over the flow cycle. Particle Image Velocimetry (PIV) has been used to characterize

Contributed by the Bioengineering Division for publication in the JOURNAL OF BIOMECHANICAL ENGINEERING. Manuscript received by the Bioengineering Division September 30, 1999; revised manuscript received May 15, 2001. Associate Editor: C. R. Ethier.

steady and pulsatile flow (by using a sinusoidal waveform) in AAA models over a range of physiological parameters [22].

Parallel to the evaluation of hemodynamic forces due to inlet flow characteristics and irregular geometries on the rigid arterial models described above, endothelial cell culture studies have been performed in order to quantify the response that the arterial wall has at the micro level. Additionally, recent investigations demonstrate the existence of diverse cell responses under low levels of shear stress, but large *shear stress gradients*. Disturbed flow patterns at different levels of fluid shear stress gradients have been found to trigger responses of the innermost layer of the tunica intima by altering intercellular communication mechanisms [23–27]. High gradients of shear stress under steady flow conditions result in a twofold increase in cell motility of in-vitro human endothelial cell monolayers [28]. The artery wall is subject to three fluid-induced forces, which are the consequence of: (*i*) fluid shear stress, (*ii*) transmural pressure, and (*iii*) wall stretching and flexion [29].

In this paper, flow patterns and their effect on wall shear stress levels and wall pressure distributions are revisited for a two-aneurysm model. To evaluate the coexistence of high and low shear stresses in a region where laminated thrombus is most likely to be promoted, we propose the quantification of hemodynamic disturbance in pulsatile flow through AAAs for average resting conditions, by means of instantaneous Wall Shear Stress Gradient (WSSG) distributions. In addition, a correlation is developed for the maximum values of wall shear stress and WSSG as a function of the time-averaged Reynolds number.

Mathematical Formulation

The geometry of the abdominal aorta with two aneurysms is shown in Fig. 1. Two converging–diverging regions define this geometry, the physical model of which has been used previously by Finol and Amon [30,31], and Guzmán et al. [15,17]. We consider pulsatile, incompressible, homogeneous, Newtonian flow in a two-aneurysm rigid-wavy-walled axisymmetric model. Although blood is actually a non-Newtonian suspension of cells in plasma, it is reasonable to model it as a Newtonian fluid in vessels greater than approximately 0.5 mm in diameter [32]. The deformed wall is represented by two sine functions as follows:

$$f(z)=\begin{cases}\left(\dfrac{D_1-D}{4}\right)\left[1+\sin\left(\dfrac{2\pi z}{L_1}-\dfrac{\pi}{2}\right)\right]+\dfrac{D}{2} & 0\leqslant z\leqslant L_1 \quad (1a)\\ \left(\dfrac{D_2-D}{4}\right)\left[1+\sin\left(\dfrac{2\pi(z-L_1)}{L_2}-\dfrac{\pi}{2}\right)\right]+\dfrac{D}{2} & L_1<z\leqslant L_1+L_2 \quad (1b)\\ \dfrac{D}{2} & L_1+L_2<z\leqslant L_T \quad (1c)\end{cases}$$

The momentum and continuity equations in axisymmetric coordinates that govern unsteady, incompressible, and Newtonian flows are given by

$$\rho\left(\frac{\partial u_z}{\partial t}+\vec{V}\cdot\nabla u_z\right)=-\frac{\partial p}{\partial z}+\left(\frac{\partial \tau_{zz}}{\partial z}+\frac{1}{r}\frac{\partial}{\partial r}(r\tau_{rz})\right) \quad (2a)$$

$$\rho\left(\frac{\partial u_r}{\partial t}+\vec{V}\cdot\nabla u_r\right)=-\frac{\partial p}{\partial r}+\left(\frac{\partial \tau_{rz}}{\partial z}+\frac{1}{r}\frac{\partial}{\partial r}(r\tau_{rr})\right) \quad (2b)$$

$$\frac{1}{r}\frac{\partial}{\partial r}(ru_r)+\frac{\partial u_z}{\partial z}=0 \quad (2c)$$

where $\vec{V}(\vec{r},t)=u_r\hat{r}+u_z\hat{z}$ is the velocity vector, and τ_{zz}, τ_{rr}, and τ_{rz} are the components of the two-dimensional stress tensor. The boundary conditions for the velocity $\vec{V}$ are given by Eq. (3). These are: no-slip at the walls (3*a*), symmetry at the centerline (3*b*), fully developed parabolic profile at the inlet (3*c*), and zero-traction outflow condition at the exit (3*d*). In mathematical form, the boundary conditions are expressed as follows:

$$\vec{V}=\vec{0}\big|_{f(z)} \quad (3a)$$

$$\frac{\partial u_r}{\partial r}=0, u_z=0\Big|_{r=0} \quad (3b)$$

$$u_z=2\overline{u}(t)\left[1-\left(\frac{2r}{D}\right)^2\right],\ u_r=0\Big|_{z=0} \quad (3c)$$

$$\frac{\partial u_r}{\partial z}=\frac{\partial u_z}{\partial z}=0\Big|_{z=L_T} \quad (3d)$$

An outflow length has been added to account for the zero-traction outflow condition, which is equivalent to half the length of the dilated portion of the artery, or 3.75 inlet diameters. Tests were performed with outflow lengths of 7.5*D* and 11.25*D* under conditions of constant flow rate, resulting in no significant changes in the flow patterns and shear stress distributions. Blood flow is simulated for average blood properties [33]: molecular viscosity $\mu=0.00319$ Pa·s and density $\rho=1{,}050$ kg/m^3. The governing equations are nondimensionalized by the factor *D*; hemodynamic indicators evaluated at the arterial wall are nondimensionalized using their corresponding magnitudes obtained for Poiseuille flow. For example, the normalized axial velocity is given by $u_z^*=u_z/u_o$, where u_o is the inlet centerline velocity; the nondimensional pressure is given by $p_w^*=(p_w-p_{\text{out}})/|\Delta p_{\max}|$, where p_w is the pressure at the wall, p_{out} is the exit pressure of 0 Pa, and $\Delta p_{\max}$ is the magnitude of the total pressure drop, $p_{\text{out}}-p_{\text{in}}$.

For pulsatile flow conditions, the inflow mean velocity is time-dependent and the volume flow rate has an oscillatory nature, as shown in Fig. 2. We represent the pulsatile flow by a discrete Fourier series based on the in-vivo measurement reported first by Mills et al. [34], which is a triphasic pulse appropriate for average resting hemodynamic conditions (generally taken for $\text{Re}_m\approx 300$

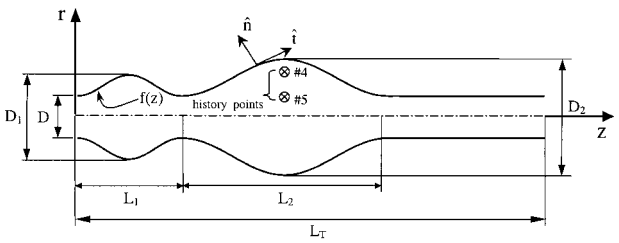

Fig. 1 Representation of the axisymmetric model of the two-aneurysm abdominal aorta, for which $L_1=2.5D$, $L_2=5D$, $L_T=11.25D$, $D_1=2D$, and $D_2=2.75D$

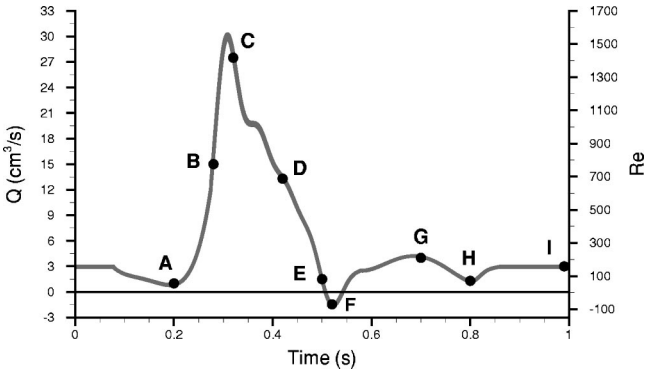

Fig. 2 Pulsatile volumetric flow rate (*Q*) and instantaneous Reynolds number (Re) for $Re_m=300$. Flow stages *A*,*B*,...,*I* are of particular importance for the evaluation of hemodynamic indicators. Peak systolic flow occurs at $t=0.31$ s and diastolic phase begins at $t=0.52$ s.

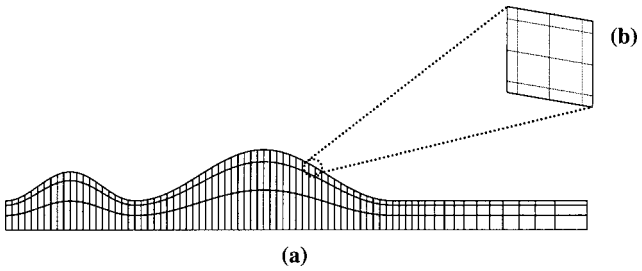

Fig. 3 Axisymmetric two-aneurysm spectral element mesh: (*a*) macroelement discretization, and (*b*) local element decomposition

and $\alpha \approx 12$, as indicated by Pedersen et al. [35,36]) in the abdominal segment of the human aorta [37]. A more recent publication by Maier et al. [38] has reported similar flow measurements in the normal human abdominal aorta using ultrasound and magnetic resonance imaging. While these in-vivo measurements result in a physiological curve that has a longer retrograde flow region, the overall description of the different flow phases of the cycle is almost identical to that resulting from the application of Mills' curve. The reader is referred to the appendix for a detailed comparison of the flow patterns and wall shear stress distributions resulting from the application of Mills' and Maier's physiological curves at moderate time-averaged flow rates.

The time dependency of the inflow mean velocity is imposed by the following Fourier representation:

$$\overline{u}(t)=A_0+\sum_{k=1}^{N}\left(A_k\cdot\cos 2\pi kt+B_k\cdot\sin 2\pi kt\right) \tag{4}$$

where $N=18$ is the number of harmonics used. The natural frequency of the pulsatile flow is set to $\omega=2\pi$ rad/s, with a period $T_P=1$ s, as shown in Fig. 2. The Womersley number, which characterizes the flow frequency, the geometry of the model, and the fluid viscous properties, is $\alpha=11.5$. The amplitude coefficient of the pulsatile flow is $\gamma=5.25$ and the peak systolic flow occurs at $t=0.31$ s. The time-averaged Reynolds number is calculated as $Re_m=D\overline{u}_m/\nu$, where $\overline{u}_m$ is the time-averaged inflow mean velocity.

The calculation of the local Wall Shear Stress Gradient (WSSG) is based on the predictor equation proposed by Lei and Kleinstreuer [27] at the cellular level, corrected from their previous work [39]:

$$\mathrm{WSSG}=\sqrt{\left(\frac{\partial\tau_w}{\partial\hat{t}}\right)^2+\left(\frac{\partial\tau_w}{\partial\hat{n}}\right)^2} \tag{5}$$

where $\hat{t}$ and $\hat{n}$ are the local tangential and normal directions to the wall, as shown in Fig. 1. The calculation of the terms within the WSSG indicator follows a different procedure than that implied in the statement of Lei's zero-tension hypothesis. It is not our intention to compare values of WSSG at the cellular level to those that would be expected at the wall of an abdominal aneurysm. Moreover, the presence of an AAA indicates a severely eroded intima (absence of endothelial lining).

Numerical Method

The governing equations, subject to the appropriate boundary conditions, are solved numerically using the Spectral Element Method (SEM) for the spatial discretization. The computational domain, shown in Fig. 3, is divided into 228 quadrilateral macroelements, with 76 in the axial direction. Mesh resolution tests have been conducted with our geometry using 304 macroelements (4 macroelements in the cross-streamwise direction). The numerical results did not reveal any significant changes when compared to the 228-macroelement mesh used to report the results of our work. The geometry and variables are isoparametrically mapped by using fifth-order polynomial expansions in each direction per macroelement. Thus, each macroelement is subdivided into a nonuniform local Cartesian grid that corresponds to 5×5 Gauss–Lobatto–Chebyshev collocation points. These points are clustered near the boundaries of the macroelements, and the transport variables evaluated at each point are expressed in terms of tensor products of high-order Lagrangian interpolants. A three-step time-splitting scheme is used for the semidiscrete formulation of the time-dependent terms in the momentum equations. The Spectral Element Method has been widely used for the Direct Numerical Simulation (DNS) of transitional flows with fast evolving temporal phenomenon and complex geometries. For more information on validation studies performed with SEM and a detailed description of the numerical method, the reader is referred to Patera [40] and Amon [41,42].

Results and Discussion

Numerical simulations for pulsatile flow are performed at time-averaged Reynolds numbers over the range $50<Re_m<300$. Re_m is defined as the time-averaged Reynolds number obtained by integrating the inlet Reynolds number over the pulsatile cycle. The instantaneous Reynolds number, $Re_i(t_j)$, is based on the inflow mean velocity at time t_j. The pressure at the exit is set to 0 Pa and, thus, all the pressure results presented are relative to this value. Results are obtained at 1/50 s intervals, but only selected flow stages considered to be the ones that represent the most important hemodynamic changes during the cycle are presented here. These stages are obtained at the last cycle of the asymptotically converged temporal solution, which is reached after a transient resulting from the application of the initial condition. The initial condition applied is the converged velocity and pressure field at the last three time steps of the simulation corresponding to the immediately lower time-averaged Reynolds number. For example, the initial condition for the $Re_m=300$ cycle is the converged velocity and pressure field at the last three time steps of the $Re_m=250$ cycle. Other types of initial condition are possible with our numerical code, but regardless of the initial condition, applied the output of a numerical simulation is the same as long as it overcomes the initial transient until the flow becomes time periodic. Therefore, a sufficient number of cycles must be performed numerically to overcome the transient period until convergence is achieved when the flow becomes time periodic; this is verified by analyzing velocity history at different points of the computational domain, as shown in Fig. 4 for $Re_m=100$. For transient simula-

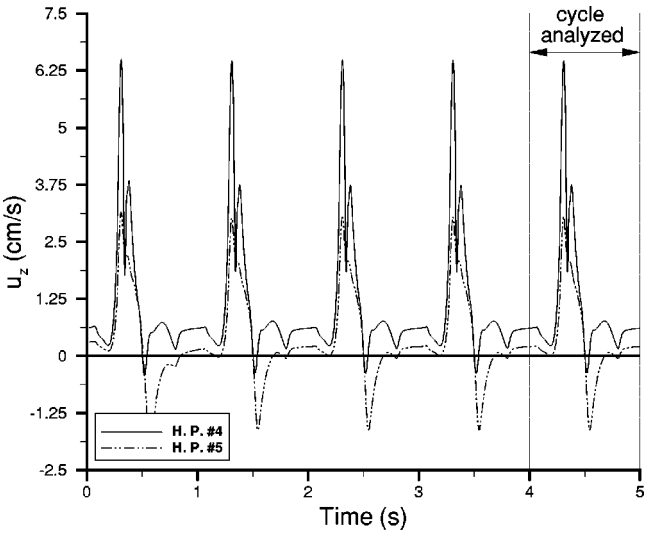

Fig. 4 Temporal evolution of the axial velocity for Re_m=100 at history points #4 and #5 (shown in Fig. 1) of the computational domain

tions, the initial value code solves the fully discrete set of governing equations at each time step by means of iterative solvers and tensor-product sum-factorization techniques.

Vortex Dynamics. Figure 5 shows streamline plots for three representative Reynolds numbers: Re_m=100 (Re_{peak}=525), Re_m=200 (Re_{peak}=1050), and Re_m=300 (Re_{peak}=1575) at eight flow stages in one pulsatile cycle. The early systolic phase of the flow cycle is characterized by a constant flow rate until t=0.08 s and an immediate deceleration until t=0.20 s. The stronger, systolic ventricular pumping begins at t=0.20 s until reaching peak flow at t=0.31 s. The residual vortices left from the last cycle are present within the two aneurysms at t=0.00 s. The fluid is subjected to a reduction of its inflow mean velocity for 0.08 s $<t\leqslant$0.20 s causing negative velocity gradients and an increase in size of the recirculation regions. A large pressure gradient follows, and the temporal acceleration of the flow is much larger for the interval 0.20 s$<t\leqslant$0.31 s than the convective deceleration originated by the proximally diverging walls of the artery ($\partial u_z/\partial t \gg \partial u_z/\partial z, \partial u_z/\partial r$). The local deceleration experienced by the fluid entering the small aneurysm is weaker than in the large aneurysm and, thus, the favorable pressure gradient ejects the vortex in the small aneurysm first, for all three Reynolds numbers. Therefore, the steady-flow-like pattern seen in frame A of Fig. 5 is no longer maintained as the high velocity core flow "pushes" the low recirculating velocity regions downstream and the flow reattaches to the wall (frame B).

For 0.31 s$<t<$0.50 s, the flow begins to decelerate temporally. A higher Reynolds number produces stronger temporal decelerations and a faster vortex formation. At t=0.32 s, near peak flow, a recirculating region fills the small aneurysm completely for Re_m=300. The vortex in the large aneurysm begins to grow for Re_m=200 and increases in size for Re_m=300. At t=0.42 s and Re_m=200, it has occupied the entire aneurysm, inducing a clockwise rotating vortex against the proximal wall. For low-Reynolds-number flows (Re_m=100), the remainder of the systolic phase is characterized by vortex growth and its downstream motion. For

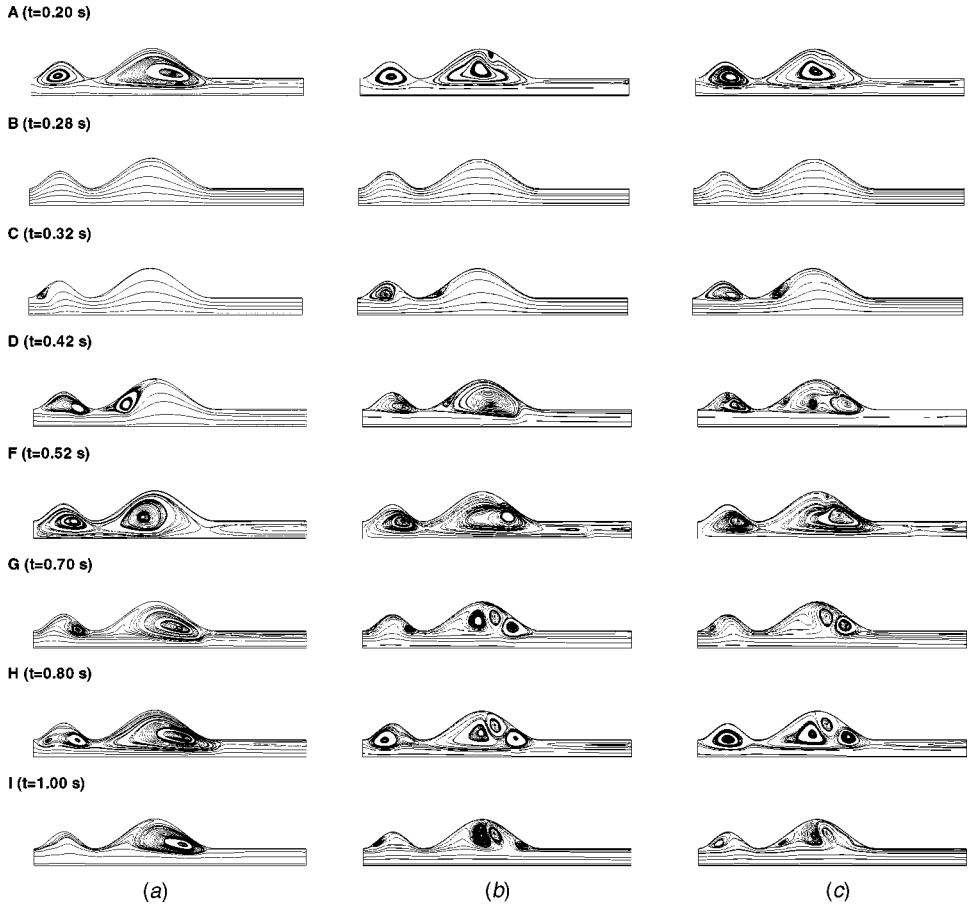

Fig. 5 Streamlines for pulsatile flow at: (*a*) Re_m=100, (*b*) Re_m=200, and (*c*) Re_m=300. The direction of the flow is from left to right.

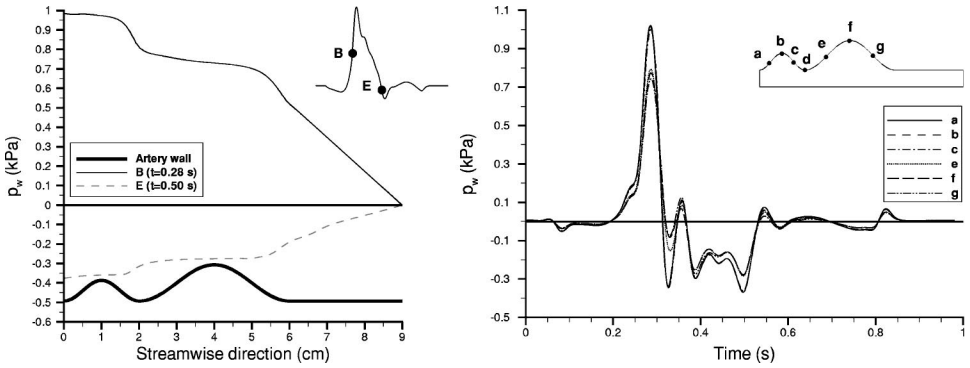

Fig. 6 Wall pressure variation for $Re_m=300$: (*a*) spatial distribution at *B*($t=0.28$ s) and *E*($t=0.50$ s); (*b*) temporal evolution at six different locations on the arterial wall

$Re_m=300$, the vortices fill the aneurysms at an early stage of systolic deceleration, so that by the start of diastole ($t=0.52$ s) they have grown in size and intensity to begin vortex shedding of the recirculation regions induced against the wall of the large aneurysm.

The negative flow period of the cycle is given by $0.51\text{ s}\leqslant t\leqslant 0.54$ s. During this interval there is a reversal of the flow direction, which is shown by the right-to-left orientation of the streamlines within the end-tube at $t=0.52$ s. For $Re_m=200$ and $Re_m=300$, there is mixing of the retrograde flow with the recirculating flow inside the aneurysms, and the few undisturbed streamlines located near the centerline indicate the significant reduction of the core flow through the artery model. The addition of an end tube to the two-aneurysm model is required to account for a zero-traction (outflow) condition farther downstream from the aneurysms, so that the imposed condition does not affect the dynamics of the flow within the deformed artery model. It is important to clarify that using a longer end tube (of length greater than 3.75 inlet diameters) would only allow for a better development of the recirculation regions downstream of the large aneurysm at specific stages of the cycle (frames *A*, *F*, and *H* in Fig. 5), which would not influence the flow dynamics upstream.

Diastole begins at $t=0.52$ s with a moderate temporal acceleration of the flow that ends at $t=0.70$ s. For $Re_m=100$, this period results in a partial ejection of the small vortex and a reduction in size of the large one. For $Re_m=200$ and $Re_m=300$, the phase is characterized by an almost complete ejection of the small vortex, the coexistence of three vortices in the large aneurysm, and the "recovery" of a core flow region at the center of the artery model in the left-to-right direction. Diastolic deceleration, which occurs for $0.70\text{ s}<t\leqslant 0.80$ s, produces an adverse pressure gradient resulting in the entrapment of the three slow-rotating vortices within the large aneurysm. For $0.80\text{ s}<t<0.86$ s, the moderate acceleration of the flow results in the ejection of the recirculation regions inside the end tube, and a reduction in size of the vortex in the small aneurysm and of the three vortices in the large aneurysm. Late diastole is characterized by a constant flow rate that lasts until the next cycle ($0.86\text{ s}\leqslant t\leqslant 1.08$ s). During this period the vortex structure does not change, a core flow region is present near the centerline with a straightening of the streamlines at the exit, and the vortices present within the aneurysms remain nearly stagnant due to the absence of flow acceleration.

Wall Pressure. The temporal accelerations and decelerations of the flow largely influence the pressure distribution at the arterial wall during the pulsatile flow cycle. The largest favorable wall pressure gradients are obtained at mid-systolic acceleration ($t=0.28$ s), and the largest adverse wall pressure gradients are obtained during late systolic deceleration ($t=0.50$ s), as shown in Fig. 6(*a*) for $Re_m=300$. However, at any given stage of the cycle, the wall pressure remains nearly constant along each aneurysm wall. At the distal ends, a characteristic rise in wall pressure is seen when the flow is decelerating or, alternatively, a sharp pressure drop when flow acceleration takes place. The converging–diverging shape of the artery seems to have a negligible effect on the pressure distribution, except for those stages of the flow where the acceleration or deceleration is small, i.e., when a change of phase of the flow waveform takes place. The change in wall pressure is also time dependent. The pulsatile nature of the flow produces oscillating wall pressure patterns similar to the imposed volumetric flow rate. In Fig. 6(*b*), the temporal evolution of the pressure at the wall is shown for six different locations on each aneurysm for $Re_m=300$. The patterns are very similar among all six locations and the distribution tends to follow the multiphasic characteristics of the pulsatile waveform.

Wall Shear Stress. Shear stresses along the artery wall for $Re_m=300$ are shown in Fig. 7. It is important to mention that this three-dimensional distribution is only a trend of the actual time-dependent variation of the wall shear stress, since it is obtained by applying a second-order graphic smoothing technique to the τ_w indicator. Therefore, the discussion that follows is for qualitative purposes only.

An oscillatory behavior characterizes the shear stress during the pulsatile cycle, having a low magnitude at the center of the aneurysm walls. Downstream of each aneurysm, there is a drop in the shear stress followed by a sharp high positive peak. These regions of low and high shear stresses are present at all times during the cycle and are time dependent, following a pattern similar to the flow waveform. The spatial variations of the wall shear stress are larger in magnitude at the distal end of the large aneurysm, denoting the effect of aneurysm diameter on this hemodynamic load.

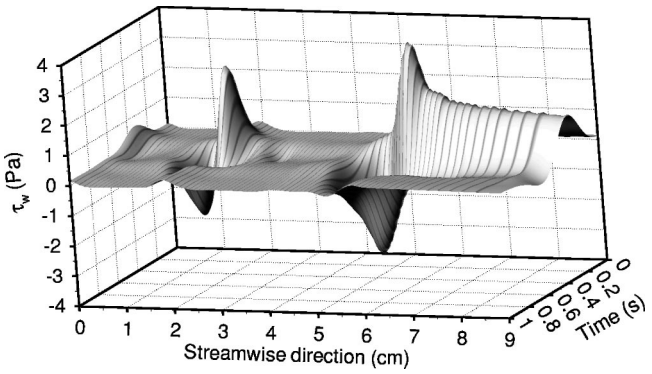

Fig. 7 Wall shear stress distribution for $Re_m=300$ as a function of time and axial location

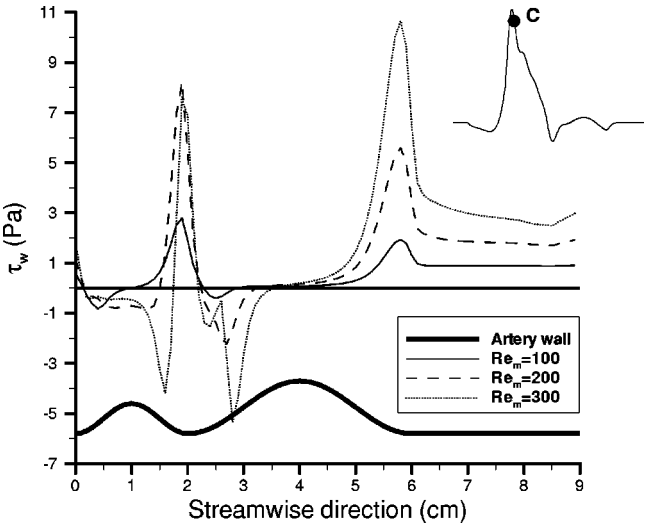

Fig. 8 Spatial variation of wall shear stresses for different time-average Reynolds numbers at *C*(t=0.32 s)

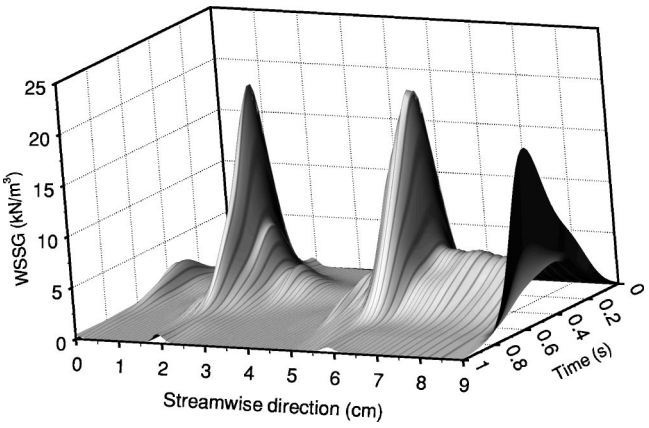

Fig. 9 Wall Shear Stress Gradient (WSSG) distribution for Re_m=300 as a function of time and axial location

Maximum positive shear stress at both distal ends occurs at peak flow, while minimum negative shear stress occurs during systolic deceleration at $t=0.40$ s.

To establish a correlation between wall shear stresses and pulsatile flow rates, we select a relevant time of the cycle to be analyzed, $t=0.32$ s, as shown in Fig. 8. For $Re_m=100$, flow separation is minimal at the diverging sections of both aneurysm and, thus, a positive shear stress distribution dominates with a typical distal-end rise in each aneurysm. The high shear stress level at this location is due to a local acceleration of the flow, which is larger in the small aneurysm, as the contraction of the streamlines in Fig. 5 clearly indicates. The relative magnitude of the shear stress increases with the Reynolds number, and for $Re_m \geqslant 150$, negative stresses are present downstream of the small aneurysm center. The recirculation regions for $Re_m=300$ extend over a wider area and larger velocity gradients occur at the wall, resulting in localized changes of shear stress of greater magnitude. The distally located peak shear stresses are obtained at about the same location for all Reynolds numbers: for the small aneurysm at $z=1.90$ cm, and for the large aneurysm at $z=5.80$ cm. Therefore, the spatial distribution of wall shear stresses for $Re_m \geqslant 150$ is similar to that for steady flow, the difference being the location where the change of sign of the stresses occurs. For steady flow, a wider area of negative shear stress dominates as the flow reattaches to the wall close to the exit. For pulsatile flow at $t=0.32$ s, the reversed flow region does not fill the large aneurysm, resulting in reattachment of the flow in the proximal half for $Re_m=200$ and $Re_m=300$. For $Re_m=300$, an instantaneous Reynolds number of $Re_i=1461$ is obtained at $t=0.32$ s, for which $\tau_{w,\max}=7.62$ Pa in the small aneurysm and $\tau_{w,\max}=10.6$ Pa in the large aneurysm. These results are 90 and 106 percent higher than their respective steady-flow counterparts at Re=1500. When the comparison is based on the same time-averaged volume flow rate, $\tau_{w,\max}$ in the small aneurysm for pulsatile flow at $Re_m=300$ is 852 percent higher than for steady flow at $Re_m=300$. Similarly, $\tau_{w,\max}$ in the large aneurysm for pulsatile flow at $Re_m=300$ is 1133 percent higher than for steady flow at the same Reynolds number.

Wall Shear Stress Gradient. In-vivo disturbed flow in localized regions of the cardiovascular system commonly subject to diagnosis of arterial diseases are typically associated with vortex structures, nonuniform fluid shear stress, and high wall pressure. The focal occurrence of this hemodynamic disturbance has been correlated in-vitro with the alignment and migration of endothelial cells, as well as changes in their metabolic functions, which include cell division rates, protein-protein interactions, and cytosolic free calcium concentrations, among others [43–47]. Nonuniform time-averaged shear stress measured experimentally at sites where irregular geometries take place in the arterial tree have led to the concept of shear stress gradient as a hemodynamic indicator of potential importance for explaining flow-induced arterial wall pathology and morphological changes in the endothelial lining. Moreover, the combination of maximum (positive) and minimum (negative) wall shear stresses at the distal end of an aneurysm under steady flow conditions has been shown to promote thrombus formation. When platelets are trapped within the recirculation region, those that have elevated histories of shear stress and a higher incidence of activation are shown to deposit at the wall in areas of low wall shear stress [10]. Therefore, evaluating wall shear stress gradients in AAAs would give an indication of the regions where high platelet deposition rates should be expected and where thrombus formation would be initiated inside the aneurysm. Consequently, we present the gradient of fluid shear stress evaluated in the tangential and normal directions to the arterial wall as a relevant hemodynamic indicator of pulsatile blood flow in AAAs.

The Wall Shear Stress Gradient (WSSG) distribution for $Re_m=300$ is shown in Fig. 9. Similarly to Fig. 7, this three-dimensional representation of WSSG is a smoothed output of the actual distribution and it is presented in this section only for a qualitative description. The low, almost constant shear stress at the center of the aneurysm walls produces a constant WSSG of near-zero magnitude during the pulsatile cycle at these locations. At the proximal (upstream) and distal (downstream) ends of each aneurysm, however, the oscillatory behavior of the WSSG distribution is characterized by spatial variations at the sites where large velocity gradients occur. The regions where high positive and low negative shear stresses coexist due to flow reattachment are subject to high WSSG values, which are maximum at $t=0.31$ s, when peak flow is obtained. Moderate levels of WSSG are obtained in both aneurysms during the accelerating (early systole and early diastole) and decelerating (late systole) phases of the cycle. This is explained by the fact that during temporal acceleration (consider $0.20\text{ s} \leqslant t \leqslant 0.30$ s, for example), vortex shedding and flow separation occur earlier in the small aneurysm, producing higher shear stresses in the distal end. Alternatively, temporal deceleration induces secondary recirculation regions within the large aneurysm (e.g., $0.32\text{ s} \leqslant t \leqslant 0.50$ s), which result in an additional change of sign in the shear stress at the wall near the point of flow reattachment. At peak values of flow rate where temporal acceleration is essentially zero ($t=0.31$ s and $t=0.52$ s), aneurysm size determines the magnitude of the shear stress distribution, resulting in

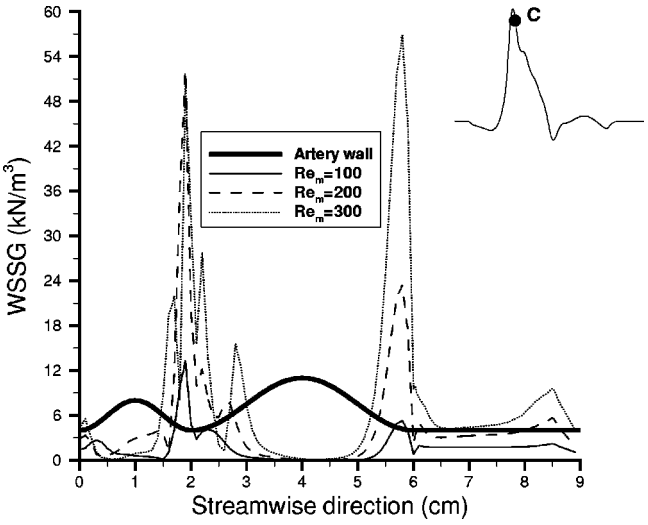

Fig. 10 Spatial variation of wall shear stress gradients for different time-average Reynolds numbers at $C(t=0.32\ \mathrm{s})$

higher WSSGs in the large aneurysm. No information is presently available in the literature on measurements of WSSGs in aneurysms.

The role of wall shear stress gradients in specific arterial diseases is not thoroughly understood yet. Our numerical results for pulsatile flow point to an intermediate stage of aneurysm growth for which disturbed flow conditions exist. The quantification of this disturbance results in three distinct regions of flow development: (1) very low wall shear stresses at the center of a bulge region; (2) high wall shear stress gradients in the distal end of each bulge; and (3) oscillating wall shear stresses and wall shear stress gradients throughout each bulge. The oscillatory nature of the WSSG at high time-averaged volume flow rates, once the aneurysm has begun to grow, produces maximum values of a periodic, pulsating hemodynamic force that may be responsible for severe sites of injury to the inner wall over a relatively long period of time. Figure 10 shows the WSSG distribution at $t=0.32$ s for different time-averaged Reynolds numbers. For $\mathrm{Re}_m=100$, the undeveloped recirculation region in the small aneurysm and the nearly attached flow pattern in the large aneurysm result in a distribution of low WSSGs, with a characteristic rise in the distal end of each aneurysm where convective acceleration plays an important role at this stage of the pulsatile flow. A uniform and almost zero WSSG exists at the center of the large aneurysm due to the nearly constant shear stress at this location. For $\mathrm{Re}_m=200$, the WSSG distribution in the small aneurysm is similar to the one in steady flow: Two peaks in the WSSG curve are obtained around the point of flow reattachment. The spatial variation of the stronger velocity gradients in the proximal end of the large aneurysm results in a WSSG greater than the inlet value. The recirculation region does not fill the aneurysm completely and, thus, a slight increase in the shear stress gradient occurs in the proximal end as opposed to the zero WSSG that characterizes a steady flow pattern. For $\mathrm{Re}_m=300$, well-developed flow recirculation within the small aneurysm results in a higher WSSG at the distal end, increasing sharply at $z=1.65$ cm, where reattachment to the wall occurs and a change of sign in the shear stress is a key factor for hemodynamic disturbance at the site. For this Reynolds number at $t=0.32$ s, $\mathrm{WSSG}_{\max}=50.9\ \mathrm{kN/m^3}$ in the small aneurysm and $\mathrm{WSSG}_{\max}=56.8\ \mathrm{kN/m^3}$ in the large aneurysm. These results are 92 and 103 percent higher than their respective steady-flow counterparts at the same instantaneous Reynolds number. Based on the time-average volume flow rates, $\mathrm{WSSG}_{\max}$ in the small aneurysm is 1250 percent higher and $\mathrm{WSSG}_{\max}$ in the large aneurysm is 847 percent higher for pulsatile flow at $\mathrm{Re}_m=300$ than for steady flow at the same Reynolds number.

Table 1 Correlation coefficients for maximum wall shear stress and wall shear stress gradient as a function of the time-averaged Reynolds number at $C(t=0.32\ \mathrm{s})$, according to Eq. (5)

		Correlation Coefficients				
Hemodynamic Parameter		$a_4 \times 10^{10}$	$a_3 \times 10^{7}$	$a_2 \times 10^{4}$	$a_1 \times 10^{2}$	$a_0 \times 10^{2}$
$\tau_{w,\max}$	small AAA	-38.76	9.88	0.95	1.22	1.54
	large AAA	0.46	-0.73	1.04	0.97	0.11
$\mathrm{WSSG}_{\max}$	small AAA	-421.35	149.21	-2.97	5.25	7.18
	large AAA	-8.51	9.30	4.22	0.20	0.01

Correlation Functions. Since the distal end of an aneurysm is subject to the highest wall shear stresses and WSSGs in the vicinity of flow reattachment, we have developed correlations for the region where aneurysm rupture is most likely to occur [48]. The correlation of wall hemodynamics with the time-averaged Reynolds number is established by a fourth-order polynomial function of the form:

$$\xi_w(t)=\sum_{i=0}^{4} a_i\,\mathrm{Re}_m^i \tag{6}$$

where $\xi_w=f(\mathrm{Re}_m,t)$ is the hemodynamic indicator evaluated at the wall (τ_w or WSSG) at a given time during the pulsatile flow cycle. Table 1 shows the coefficients (in the appropriate units) resulting from the correlations at $t=0.32$ s. These correlations are

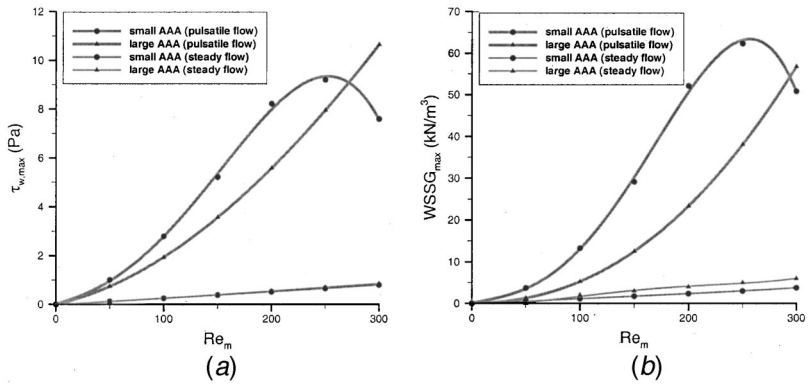

Fig. 11 Comparison of wall hemodynamics as a function of time-average Reynolds number for steady and pulsatile flow at $C(t=0.32\ \mathrm{s})$: (*a*) maximum wall shear stress; (*b*) maximum wall shear stress gradient

used to compare the variation of the maximum wall shear stress and WSSG with Re_m, for pulsatile flow at $t=0.32$ s and for steady flow, as shown in Fig. 11.

Figure 11(*a*) shows a monotonic increase of the maximum (positive) wall shear stress for the large aneurysm, similar to the steady flow distribution. The maximum shear stress in the large aneurysm is greater than the one in the small aneurysm only for $Re_m \geq 270$. The temporal development of vortex structures discussed earlier accounts for this behavior. For $Re_m < 270$, the fact that the recirculation region begins to fill in the small aneurysm before flow separation takes place in the large aneurysm indicates that, at $t=0.32$ s, the velocity gradients in the small aneurysm are stronger than in the large aneurysm. For higher Reynolds numbers ($Re_m \geq 270$), where flow separation occurs before peak flow (e.g., $t_{separation}=0.29$ s for $Re_m=300$), reversed flow already fills the proximal half of the large aneurysm at $t=0.30$ s. This results in a higher maximum shear stress in the large aneurysm. A similar pattern is shown for $WSSG_{max}$ in Fig. 11(*b*), where the maximum WSSG in the large aneurysm is greater than the one in the small aneurysm only for $Re_m \geq 290$. The intersection of the $WSSG_{max}$ and $\tau_{w,max}$ curves does not occur at the same Re_m; this is explained by evaluating the contribution of the individual terms of the WSSG indicator, as given by Eq. (5). In the range $270 \leq Re_m \leq 290$, the WSSG in the tangential direction ($\partial \tau_w / \partial \hat{t}$) is greater in the large aneurysm than in the small aneurysm. The shear stress gradient in the direction normal to the wall ($\partial \tau_w / \partial \hat{n}$), however, is much smaller in the distal end of the large aneurysm, where $WSSG_{max}$ occurs. The distribution of the streamlines at this location for $t=0.32$ s indicates a region of forward flow, since the vortex is at an early stage of development, closer to the diverging wall of the large aneurysm. Therefore, the contribution of the $\partial \tau_w / \partial \hat{n}$ term is significant in the pattern of the $WSSG_{max}$ distribution for the range $270 \leq Re_m \leq 290$. A comparison between steady and pulsatile flow maximum wall stresses indicates that the wall shear stress in the small aneurysm for pulsatile flow at $t=0.32$ s is up to 15.8 times the wall shear stress for steady flow; this occurs at $Re_m=200$. Additionally, the $WSSG_{max}$ for pulsatile flow in the small aneurysm is 9.5 times greater than its steady flow counterpart at $Re_m=300$. For the large aneurysm, there is a monotonic increase of this $\tau_{w,max}$ and $WSSG_{max}$ differential with Re_m.

Conclusions

The vortex dynamics induced by pulsatile blood flow in aneurysms is characterized by means of a sequence of different flow stages in one period of the pulsatile flow cycle. The following five distinct flow phases depict the Reynolds number-dependent and aneurysm-size-dependent vortex structures:

(1) *Early systolic acceleration* involves sweeping of vortices, left from the previous cycle, out of the aneurysms, resulting in attached flow patterns. Vortices in the small aneurysm are swept earlier than in the large aneurysm.

(2) *Late systolic acceleration* is characterized by attached flow for low time-average Reynolds numbers ($Re_m \leq 100$). For high Re_m, the decrease in the temporal acceleration of the fluid upon reaching peak flow causes flow separation in the proximal ends of both aneurysms. The annular vortex forms earlier in the small aneurysm.

(3) *Systolic deceleration* is characterized by vortex growth and translation of vortex centers downstream. For high Re_m, secondary clockwise-rotating vortices are induced at the center of both aneurysms, once the main recirculation regions grow to full size.

(4) *Early diastole* is characterized by partial shedding of the vortex structures left from systole, driven by a favorable pressure gradient. The recirculation regions are reduced considerably in size, as the flow attempts to reattach to the wall.

(5) *Late diastole* involves fairly constant size vortices within both aneurysms. For high Re_m, secondary vortices coexist with the main recirculation region at the center of the large aneurysm.

The temporal evolution of the flow pattern influences the spatial distribution and oscillatory behavior of hemodynamic indicators such as wall pressure, wall shear stress, and WSSG. At $t=0.32$ s, the highest wall shear stress and WSSG levels analyzed in this work are obtained at the distal end of both aneurysms. The maximum wall shear stress during the pulsatile flow cycle for $Re_m=300$ is 852 percent higher in the small aneurysm and 1133 percent higher in the large aneurysm, than the corresponding maximum wall shear stresses obtained for steady flow at $Re=300$. Similarly, the maximum WSSG for $Re_m=300$ is 1250 percent higher in the small aneurysm and 847 percent higher in the large aneurysm, than the respective maximum WSSGs obtained for steady flow at the same time-averaged flow rate. This indicates the importance of performing physiologically realistic pulsatile flow simulations to predict accurately the maximum hemodynamic stresses experienced by the arterial wall at the distal end of an aneurysm. Time-dependent flow results demonstrate that the converging region of an aneurysm is cyclically exposed to high and low hemodynamic wall stresses. These stresses oscillate in time and are higher for a large aneurysm (i.e., greater maximum diameter and length) than for a small aneurysm, at the same time-averaged Reynolds number.

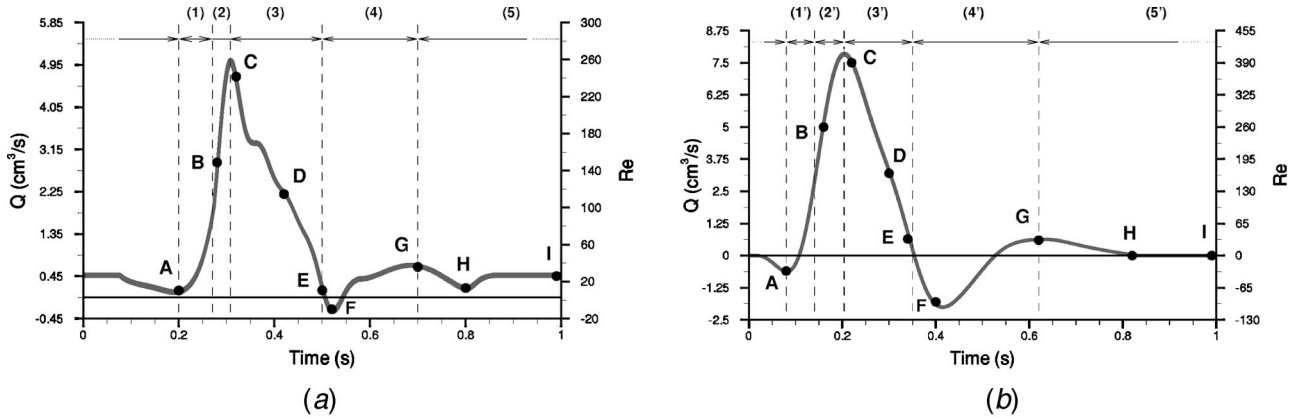

Fig. 12 Pulsatile volumetric flow rate (*Q*) and instantaneous Reynolds number (Re) for $Re_m=50$, corresponding to: (*a*) Mills' [34] physiological resting curve obtained from velocity probe measurements and (*b*) Maier's [38] in-vivo flow curve obtained using an MRI technique. Flow stages (1)–(5) are described in the Conclusions section and also apply to Fig. 2.

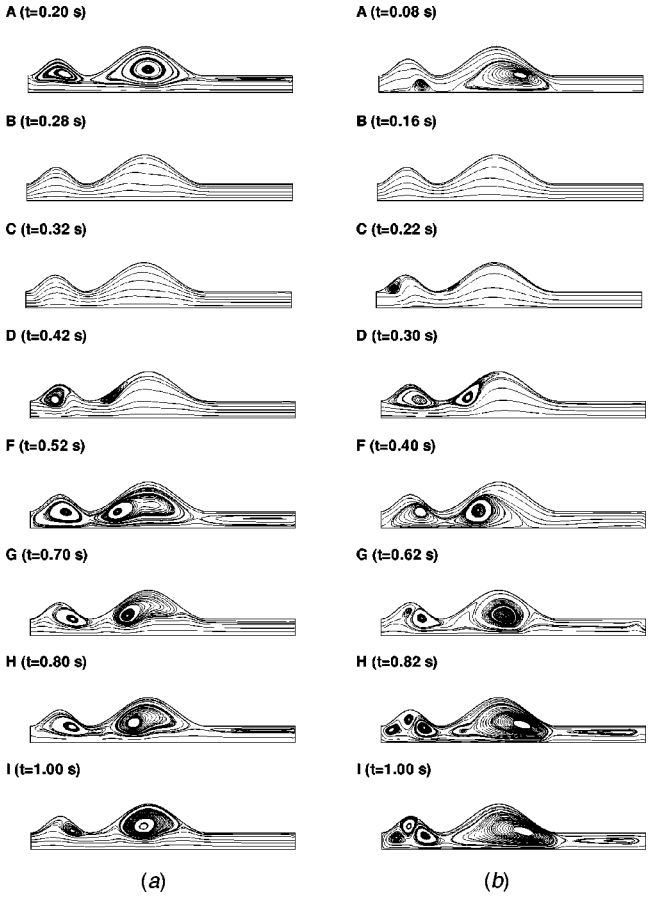

Fig. 13 Streamlines for pulsatile flow at Re_m=50 resulting from the application of: (*a*) Mills' resting curve and (*b*) Maier's in-vivo curve. The direction of the flow is from left to right.

It is unlikely that an aneurysm of medium or large size ($D > 4.5$ cm) would be axisymmetric. AAAs in an advanced stage of growth are truly asymmetric, due to the presence of tissue surrounding the abdominal aorta and to the vertebral column located posterior to this artery segment. This makes a large AAA less fusiform and causes it to grow apart from the lumen's centerline, accounting for a major anterior dilation and a more flat posterior surface. Therefore, the conclusions drawn on the basis of these axisymmetric hemodynamic stress calculations may not hold true for real three-dimensional asymmetric models. Further investigation based on asymmetric aneurysm models is currently been conducted using a novel formulation for the calculation of three-dimensional wall shear stresses.

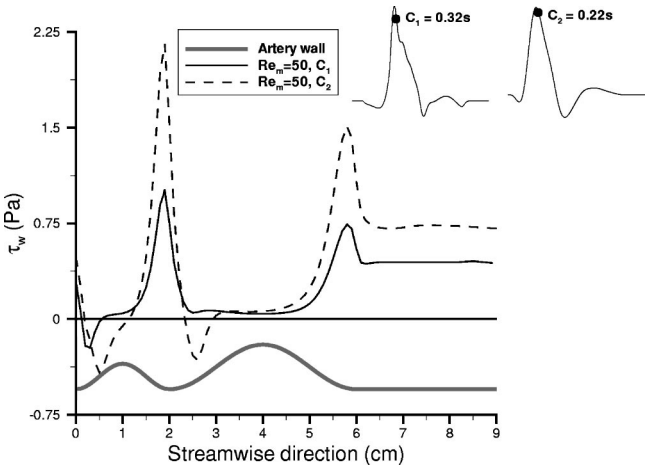

Fig. 14 Wall shear stress distributions at stage *C* (near peak flow) for Re_m=50 resulting from the application of Mills' (stage C_1) and Maier's (stage C_2) curves. Peak flow is achieved at different times in each flow curve.

Acknowledgments

The authors gratefully acknowledge the financial support of the National Science Foundation grant CTS-9630801, the Whitaker Foundation grant RG-96-0202, and the Pennsylvania Infrastructure Technology Alliance Partnership from the Commonwealth of Pennsylvania's Department of Community and Economic Development.

Appendix

Discussion on Choice of Flow Waveform. This appendix presents a detailed discussion on the choice of the flow curve represented by a discrete Fourier series in the Mathematical Formulation section and its comparison with a similar curve reported by Maier et al. [38]. The comparison is based on the numerical simulation of pulsatile flow for a moderate time-averaged Reynolds number (Re_m=50), for which Maier's curve has also been discretized in a Fourier series.

The corresponding time-dependent flow rate using Mills' curve for Re_m=50 is shown in Fig. 12(*a*). Applying Eq. (4), Maier's curve is represented by using $N=9$ harmonics. The natural frequency of the pulsatile flow is set to $\omega = 2\pi$ rad/s, with a period $T_P = 1$ s, as shown in Fig. 12(*b*). The corresponding Womersley number is $\alpha = 11.5$, the amplitude coefficient of this waveform is $\gamma = 8.25$, and the peak systolic flow occurs at $t = 0.21$ s. While the time-averaged flow rate is the same for both waveforms, Maier's curve differs primarily from Mills' in that it provides a four-times-longer period of retrograde flow and the amplitude coefficient is

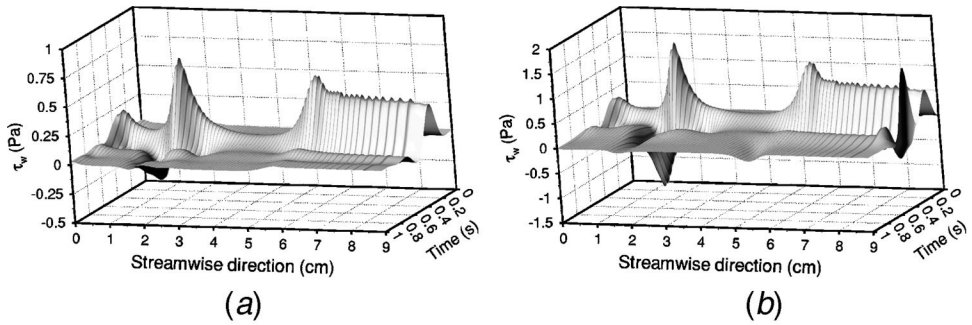

Fig. 15 Wall shear stress distribution for Re_m=50 as a function of time and axial location for: (*a*) Mills' flow curve and (*b*) Maier's flow curve

57 percent larger. Therefore, $Re_{peak}=263$ in Fig. 12(*a*) and $Re_{peak}=413$ in Fig. 12(*b*). For most stages, this yields flow patterns that are dissimilar in the number of recirculation regions within each bulge, as shown in Fig. 13. However, the five distinct flow phases illustrated in Fig. 12(*a*) can also be defined in Fig. 12(*b*) using a different time scale, and described for Maier's waveform as in the preceding Conclusions section. The flow phases are:

(1′) *Early systolic acceleration* involves sweeping of vortices, left from the early retrograde flow stage, out of the aneurysms, resulting in attached flow patterns. Vortices in the small aneurysm are swept earlier than in the large aneurysm.

(2′) *Late systolic acceleration* is characterized by attached flow for low time-average Reynolds numbers ($Re_m<100$).

(3′) *Systolic deceleration* is characterized by vortex growth and translation of vortex centers downstream.

(4′) *Early diastole* is characterized by a weak shedding of the vortex structures left from the retrograde flow region, driven by a favorable pressure gradient.

(5′) *Late diastole* involves fairly constant size vortices within both aneurysms. For low time-average Reynolds numbers, three vortices coexist within the small aneurysm.

Figure 14 shows the wall shear stress distribution at stage C for both waveforms. This is the stage closest to peak flow, for which the highest wall stresses are obtained during the pulsatile cycle. The maximum shear stress in each aneurysm is higher for Maier's curve, since the instantaneous flow rate at this stage is 64 percent larger than for Mills' curve. Early vortex development is seen seen in the large aneurysm at stage C_2, which accounts for the negative wall shear stress in the proximal end of the aneurysm. The pattern followed by both distributions is very similar, as attached flow is obtained for most of the dilated wall. The almost identical pattern in the shear stress distributions obtained by applying both physiological waveforms can be seen in Fig. 15 as a function of time and axial direction.

The results of the comparison of Mills' and Maier's curves in terms of flow patterns and wall shear stresses at moderate time-average Reynolds numbers indicate the validity of Mills' study, still widely referenced in the literature today. Through novel non-invasive techniques, Maier and colleagues have made important contributions to the field of in-vivo blood flow measurement, also producing waveforms for medium exercise and exercise conditions [35,36].

Nomenclature

AAA = Abdominal Aortic Aneurysm
D = inlet diameter of two-aneurysm model
D_1 = maximum diameter of small aneurysm $=2D$
D_2 = maximum diameter of large aneurysm $=2.75D$
L_1 = length of small aneurysm $=2.5D$
L_2 = length of large aneurysm $=5D$
P = blood pressure
$\overline{Q}$ = time-averaged volumetric flow rate $=\pi(D^2/4)\overline{u_m}$
r = radial coordinate measured from the model symmetry axis
Re = Reynolds number $=D\overline{u}/\nu$
Re_m = time-averaged Reynolds number
Re_{peak} = instantaneous Reynolds number at peak flow ($t=0.31$ s)
t = time
$\hat{t},\hat{n}$ = local tangential and normal directions to the wall
T_P = time period of pulsatile cycle
$\overline{u_m}$ = time-averaged inflow mean velocity
$\vec{V}$ = velocity vector
WSSG = Wall Shear Stress Gradient
z = longitudinal coordinate measured from the inlet
α = Womersley number $=(D/2)\sqrt{\omega/\nu}$
γ = amplitude coefficient of pulsatile flow $=Re_{peak}/Re_m$
μ = molecular viscosity of blood
ν = kinematic viscosity of blood $=\mu/\rho$
ρ = blood density
τ = fluid shear stress
ω = frequency of pulsatile flow $=2\pi/T_P$

Subscript

w = indicates a parameter evaluated at the wall

References

[1] Ernst, C., 1993, "Abdominal Aortic Aneurysm," N. Engl. J. Med., **328**, No. 16, pp. 1167–1172.
[2] Wille, S., 1981, "Pulsatile Pressure and Flow in an Arterial Aneurysm Simulated in a Mathematical Model," J. Biomed. Eng., **3**, pp. 153–158.
[3] Perktold, K., Gruber, K., Kenner, T., and Florian, H., 1984, "Calculation of Pulsatile Flow and Particle Paths in an Aneurysm-Model," Basic Res. Cardiol., **79**, pp. 253–261.
[4] Perktold, K., 1987, "On the Paths of Fluid Particles in an Axisymmetrical Aneurysm," J. Biomech., **20**, No. 3, pp. 311–417.
[5] Fukushima, T., Matsusawa, T., and Homma, T., 1989, "Visualization and Finite Element Analysis of Pulsatile Flow in Models of the Abdominal Aortic Aneurysm," Biorheology, **26**, pp. 109–130.
[6] Taylor, T., and Yamaguchi, T., 1994, "Three-Dimensional Simulation of Blood Flow in an Abdominal Aortic Aneurysm—Steady and Unsteady Flow Cases," ASME J. Biomech. Eng., **116**, pp. 89–97.
[7] Elger, D., Slippy, J., Budwig, R., Khraishi, T., and Johansen K., 1995, "A Numerical Study of the Hemodynamics in a Model Abdominal Aortic Aneurysm (AAA)," *Proc. ASME Symposium on Biomedical Fluids Engineering*, R. A. Gerbsch and K. Ohba, eds., ASME FED-Vol. 212, pp. 15–22.
[8] Khraishi, T., Elger, D., Budwig, R., and Johansen K., 1996, "The Effects of Modeling Parameters on the Hemodynamics of an Abdominal Aortic Aneurysm (AAA)," *Proc. 1996 ASME Fluids Engineering Division Summer Meeting*, ASME FED-Vol. 237, pp. 349–356.
[9] Schoephoerster, R., Oynes, F., Nunez, G., Kapadvanjwala, M., and Dewanjee, M., 1993, "Effects of Local Geometry and Fluid Dynamics on Regional Platelet Deposition on Artificial Surfaces," Arterioscler. Thromb., **13**, No. 12, pp. 1806–1813.
[10] Bluestein, D., Niu, L., Schoephoerster, R., and Dewanjee, M., 1996, "Steady Flow in an Aneurysm Model: Correlation Between Fluid Dynamics and Blood Platelet Deposition," ASME J. Biomech. Eng., **118**, pp. 280–286.
[11] Guzmán, A., and Amon, C., 1996, "Dynamical Flow Characterization of Transitional and Chaotic Regimes in Converging–Diverging Channels," J. Fluid Mech., **321**, pp. 25–57.
[12] Amon, C., Guzmán, A., and Morel, B., 1996, "Lagrangian Chaos, Eulerian Chaos, and Mixing Enhancement in Converging–Diverging Channel Flows," Phys. Fluids, **8**, No. 5, pp. 1192–1206.
[13] Rodkiewicz, C., Viswanath, N., and Zajac, S., 1995, "On the Abdominal Aortic Aneurysm: Numerical and In Vitro Experimental Study," *Proc. 1st 1995 Regional Conference IEEE Engineering in Medicine and Biology Society and 14th Conference of the Biomedical Engineering Society of India*, pp. 2.86–2.87.
[14] Viswanath, N., Zajac, S., and Rodkiewicz, C., 1997, "On the Abdominal Aortic Aneurysms: Pulsatile State Considerations," Med. Eng. Phys., **19**, No. 4, pp. 343–351.
[15] Guzmán, A., Moraga, N., and Amon, C., 1997, "Pulsatile Non-Newtonian Flow in a Double Aneurysm," *1997 Advances in Bioengineering*, ASME BED-Vol. 36, pp. 87–88.
[16] Moraga, N., Guzmán A., and Rosas, C., 1997, "Mecánica de Fluidos No Newtonianos de Flujo Transiente en Tubería con Sección Transversal Variable en el Espacio," *VI Congreso La Ingeniería en la Industria del Cobre*, Universidad de Antofagasta, Chile, pp. 167–175.
[17] Guzmán, A., Moraga, N., Muñoz, G., and Amon, C., 1997, "Pulsatile Non-Newtonian Flow in a Converging–Diverging Tube," AIChE Symp. Series, **93**, No. 314, pp. 288–294.
[18] Egelhoff, C., Budwig, R., Elger, D., and Khraishi, T., 1997, "A Model Study of Pulsatile Flow Regimes in Abdominal Aortic Aneurysms," *Proc. 1997 ASME Fluids Engineering Division Summer Meeting*, FED-Vol. 21, pp. 1–8.
[19] Egelhoff, C., Budwig, R., Elger, D., Khraishi, T., and Johansen, K., 1999, "Model Studies of the Flow in Abdominal Aortic Aneurysms During Resting and Exercise Conditions," J. Biomech., **32**, pp. 1319–1329.
[20] Peattie, R., and Bluth, E., 1998, "Experimental Study of Pulsatile Flows in Models of Abdominal Aortic Aneurysms," *Proc. 20th Annual International Conference of the IEEE Engineering in Medicine and Biology Society*, **20**, No. 1, pp. 367–370.
[21] Peattie, R., Cooper, J., and Day, A., 1999, "Computational Investigation of Pulsatile Flows and Wall Stresses in Models of Abdominal Aortic Aneurysms," *Proc. 1st Joint BMES/EMBS Conference*, p. 305.
[22] Yu, S., 2000, "Steady and Pulsatile Flow Studies in Abdominal Aortic Aneurysm Models Using Particle Image Velocimetry," Int. J. Heat Fluid Flow, **21**, pp. 74–83.
[23] Satcher, R., Bussolari, S., Gimbrone, M., and Dewey, C., 1992, "The Distribution of Forces on Model Arterial Endothelium Using Computational Fluid Dynamics," ASME J. Biomech. Eng., **114**, pp. 309–316.
[24] Satcher, R., and Dewey, C., 1996, "Theoretical Estimates of Mechanical Prop-

erties of the Endothelial Cell Cytoskeleton,'' Biophys. J., **71**, pp. 109–118.
[25] DePaola, N., Gimbrone, M., Davies, P., and Dewey, C., 1992, ''Vascular Endothelium Responds to Fluid Shear Stress Gradients,'' Arterioscler. Thromb., **12**, No. 11, pp. 1254–1257.
[26] Davies, P., Mundel, T., and Barbee, K., 1995, ''A Mechanism for Heterogeneous Endothelial Responses to Flow In Vivo and In Vitro,'' J. Biomech., **28**, No. 12, pp. 1553–1560.
[27] Lei, M., and Kleinstreuer, C., 1996, ''The Zero-Tension Hypothesis for the Mechanism of Atherogenesis and the Wall Shear Stress Gradient (WSSG) Predictor Equation,'' *1996 Advances in Bioengineering*, ASME BED-Vol. 33, pp. 211–212.
[28] Tardy, Y., Resnick, N., Nagel, T., Gimbrone, M., Dewey, C., 1997, ''Shear Stress Gradients Remodel Endothelial Monolayers in Vitro via a Cell Proliferation-Migration-Loss Cycle,'' Arterioscler., Thromb., Vasc. Biol., **17**, pp. 3102–3106.
[29] Graboswki, E., 1995, ''Thrombolysis, Flow, and Vessel Wall Interactions,'' J. Vascular Interventional Radi. **6**, No. 6, Pt 2 pp. 25S–29S.
[30] Finol, E., and Amon, C., 2000, ''Pulsatile Flow Hemodynamics in Abdominal Aortic Aneurysms,'' *Proc. V International Congress of Numerical Methods in Engineering and Applied Sciences—CIMENICS 2000*, Troyani, N., and Cerrolaza, M., eds., Sociedad Venezolana de Métodos Numéricos en Ingeniería, Caracas, Venezuela, pp. CI81–CI90.
[31] Finol, E., and Amon, C., 2000, ''Momentum Transfer in Abdominal Aortic Aneurysms: The Effect of Aneurysm Size in Steady Flow Hemodynamics,'' *Proc. 34th ASME National Heat Transfer Conference—NHTC 2000*, No. NHTC2000-12205.
[32] McDonald, D., 1960, *Blood Flow in Arteries*, Wilkins & Wilkins, Baltimore, MD.
[33] Albritton, E., 1951, *Standard Values in Blood*, United States Air Force, Wright Air Development Center, pp. 5–7.
[34] Mills, C., Gabe, I., Gault, J., Mason, D., Ross, J. Jr., Braunwald, E., and Shillingford, J., 1970, ''Pressure-Flow Relationships and Vascular Impedance in Man,'' Cardiovasc. Res., **4**, pp. 405–417.
[35] Pedersen, E., Yoganathan, A., and Lefebvre, X., 1992, ''Pulsatile Flow Visualization in a Model of the Human Abdominal Aorta and Aortic Bifurcation,'' J. Biomech., **25**, No. 8, pp. 935–944.
[36] Pedersen, E., Sung, H., Burlson, A., and Yoganathan, A., 1993, ''Two-Dimensional Velocity Measurements in a Pulsatile Flow Model of the Normal Abdominal Aorta Simulating Different Hemodynamic Conditions,'' J. Biomech., **26**, No. 10, pp. 1237–1247.
[37] Milnor, W., 1989, *Hemodynamics*, Wilkins & Wilkins, Baltimore, MD, 2nd ed.
[38] Maier, S., Meier, D., Boesiger, P., Moser, U., and Vieli, A., 1989, ''Human Abdominal Aorta: Comparative Measurements of Blood Flow With MR Imaging and Multigated Doppler US,'' Radiology, **171**, pp. 487–492.
[39] Lei, M., Kleinstreuer, C., and Truskey, G., 1995, ''Numerical Investigation and Prediction of Atherogenic Sites in Branching Arteries,'' ASME J. Biomech. Eng., **117**, pp. 350–357.
[40] Patera, A., 1984, ''A Spectral Element Method for Fluid Dynamics: Laminar Flow in a Channel Expansion,'' J. Comput. Phys., **54**, pp. 468–488.
[41] Amon, C., 1993, ''Spectral Element-Fourier Method for Transitional Flows in Complex Geometries,'' AIAA J., **31**, No. 1, pp. 42–48.
[42] Amon, C., 1995, ''Spectral Element-Fourier Method for Unsteady Forced Convective Heat Transfer in Complex Geometry Flows,'' J. Thermophys. Heat Transfer, **9**, No. 2, pp. 247–253.
[43] Davies, P., 1997, ''Mechanisms Involved in Endothelial Responses to Hemodynamic Forces,'' Atherosclerosis, **131**, Suppl pp. S15–S17.
[44] Davies, P., Dewey, C., Bussolari, S., Gordon, E., and Gimbrone, M., 1984, ''Influence of Hemodynamic Forces on Vascular Endothelial Function,'' J. Clin. Invest., **73**, pp. 1121–1129.
[45] Davies, P., Remuzzi, A., Gordon, E., Dewey, C., and Gimbrone, M., 1986, ''Turbulent Fluid Shear Stress Induces Vascular Endothelial Cell Turnover In Vitro,'' Proc. Natl. Acad. Sci. U.S.A., **83**, pp. 2114–2117.
[46] Dewey, C., Bussolari, S., Gimbrone, M., and Davies, P., 1981, ''The Dynamic Response of Vascular Endothelial Cells to Fluid Shear Stress,'' ASME J. Biomech. Eng., **103**, pp. 177–185.
[47] Shen, J., Luscinkas, F., Connolly, A., Dewey, C., and Gimbrone, M., 1992, ''Fluid Shear Stress Modulates Cytosolic Free Calcium in Vascular Endothelial Cells,'' Am. J. Physiol., **262**, No. 2, Pt. 1, pp. C384–C390.
[48] Muraki, N., 1983, ''Ultrasonic Studies of the Abdominal Aorta With Special Reference to Hemodynamic Considerations on Thrombus Formation in the Abdominal Aortic Aneurysm,'' J. Jap. College Angiol., **23**, pp. 401–413.